

# An Integrated Hybrid Silicon Multiwavelength AWG Laser

Géza Kurczveil, Martijn J. R. Heck, *Member, IEEE*, Jonathan D. Peters, John M. Garcia, Daryl Spencer, and John E. Bowers, *Fellow, IEEE*

**Abstract**—The first integrated multiwavelength laser based on an arrayed waveguide grating (AWG) fabricated on a silicon-on-insulator wafer is presented. It consists of Fabry–Perot cavities integrated with hybrid silicon amplifiers and an intracavity filter in the form of an AWG with a channel spacing of 360 GHz. Four-channel lasing operation is shown. Single-sided fiber-coupled output powers as high as  $35 \mu\text{W}$  are measured. The device shows subnanosecond rise and fall times, and direct modulation at 1 GHz gives an open eye with an extinction ratio of 7.7 dB.

**Index Terms**—Semiconductor laser, silicon-on-insulator (SOI) technology, silicon photonics.

## I. INTRODUCTION

OPTICAL interconnects have the potential of replacing electrical interconnects for on-chip and off-chip applications as they offer higher bandwidth and lower power operation than their electrical counterparts [1], [2]. Wavelength division multiplexing (WDM) is one approach to take advantage of the bandwidth offered by optical interconnects [3], and multiwavelength lasers (MWLs) are an important part of WDM transmitters.

There are several approaches to make an MWL. One is to multiplex several single-wavelength lasers (for example, distributed feedback lasers) with an arrayed waveguide grating (AWG). While such configurations give control over the lasing wavelength, they are complex to operate as each channel has to be aligned to an AWG passband. Another approach is to make an AWG laser. Here, the AWG is used not only as a multiplexer but also as an intracavity grating. These devices are easier to operate as the lasing wavelength is determined by the bandpass characteristics of the AWG, so no external tuning is required. The schematic diagram of such a device is shown in Fig. 1(a).

So far, AWG lasers have been fabricated only on InP substrates [4], [5]. Devices with integrated modulators have also been demonstrated [6]. While InP does offer high gain, and thus low lasing thresholds, making such a device on silicon is of great interest as silicon-on-insulator (SOI) wafers give a higher

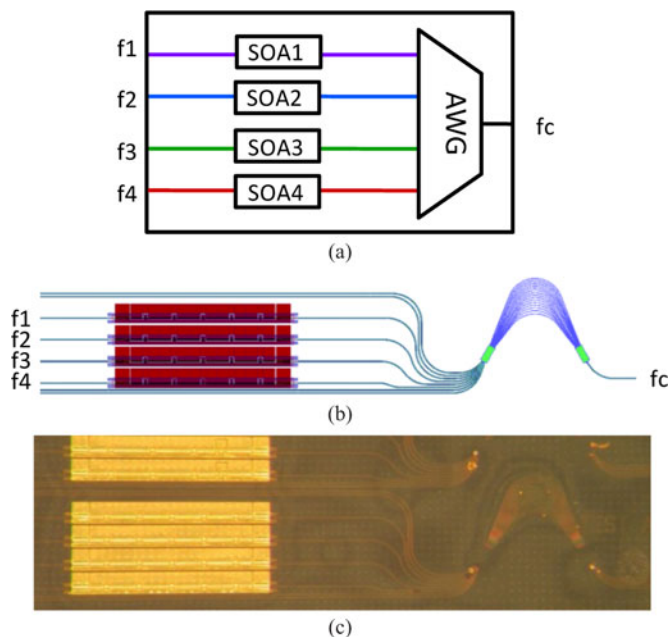


Fig. 1. (a) Schematic diagram of an AWG laser with four channels. (b) Schematic diagram of the fabricated chip. The AWG has eight channels. Four of the eight channels have hybrid silicon SOAs. (c) Optical photograph of the fabricated chip. The sample is covered with thick SU8 polymer that decreases the contrast of the image.

index contrast structure enabling more compact devices. In addition, mature CMOS technology can be used to define low-loss waveguides [7] with high yield and reproducibility at a low cost. High-resolution AWGs on SOI have been fabricated on a small footprint as shown by a 50-channel AWG on an  $8 \text{ mm} \times 8 \text{ mm}$  footprint [8].

The hybrid silicon platform is an attractive platform as it combines low-loss silicon waveguides with active elements. While many single-wavelength devices have been fabricated on this platform [9], no AWG-based MWLs have been demonstrated so far. This paper presents the first AWG-based MWL on the hybrid silicon platform. The design and the fabrication of the device are described in Section II, while the device characterization is shown in Section III. This paper concludes with Section IV.

## II. DEVICE DESIGN AND FABRICATION

The layout of the fabricated hybrid silicon AWG laser is shown in Fig. 1(b). The device is 5 mm in length and consists of a Fabry–Perot cavity with an AWG. The AWG has eight channels, a channel spacing of 360 GHz, and it measures  $900 \mu\text{m} \times$

Manuscript received December 1, 2010; revised January 30, 2011; accepted January 31, 2011. Date of publication March 14, 2011; date of current version December 7, 2011. This work was supported by the Defense Advanced Research Projects Agency under the LASOR program under Award W911NF-04-9-0001.

The authors are with the University of California, Santa Barbara, CA 93106 USA (e-mail: gezak22@hotmail.com; mheck@ece.ucsb.edu; peters@ece.ucsb.edu; johngarcia@ece.ucsb.edu; darylspencer@umail.ucsb.edu; bowers@ece.ucsb.edu).

Color versions of one or more of the figures in this paper are available online at <http://ieeexplore.ieee.org>.

Digital Object Identifier 10.1109/JSTQE.2011.2112639

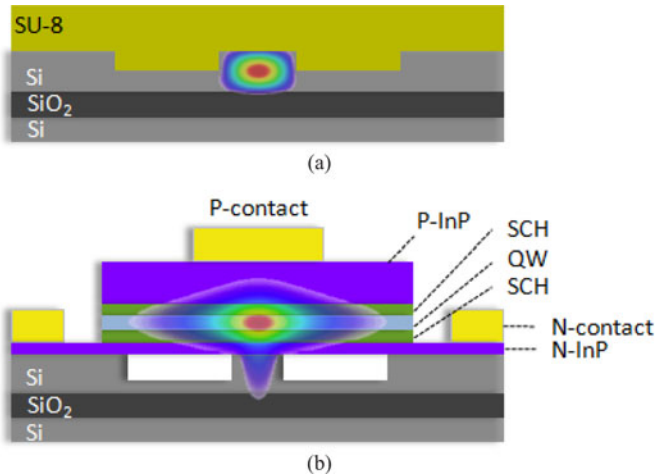


Fig. 2. Cross section of the (a) passive waveguide and (b) hybrid silicon waveguide. The mode profiles are also shown.

700  $\mu\text{m}$ . A III–V die was bonded to the SOI die and 1-mm-long hybrid silicon semiconductor optical amplifiers (SOAs) on four of the eight channels were defined by further processing. By biasing SOAs 1–4 above threshold, four lasing cavities are formed between facets f1–f4 and the common output facet fc in Fig. 1(b). An optical photograph of the fabricated device is shown in Fig. 1(c).

A schematic diagram of the cross section of a hybrid silicon waveguide is shown in Fig. 2. It consists of a III–V epitaxial layer stack that is bonded to an SOI die.

The SOI sample has a 1- $\mu\text{m}$ -thick buried oxide layer that is thick enough to prevent light from leaking into the substrate and thin enough to allow heat transfer to the substrate. The top silicon layer is 0.7  $\mu\text{m}$  high while the rib etch is 0.44  $\mu\text{m}$  deep. These parameters were chosen to allow the fabrication of compact devices (200- $\mu\text{m}$  bending radii) while keeping bending and waveguide leakage losses far below the loss due to sidewall roughness. In the hybrid region, the silicon waveguide is 1  $\mu\text{m}$  wide to maximize the overlap of the mode with the quantum wells, thus maximizing the gain. In the passive region, the waveguide is 2  $\mu\text{m}$  wide to reduce the overlap of the mode with the sidewall, thus reducing the loss by  $\sim 5$  to  $\sim 1$  dB/cm when compared to a 1- $\mu\text{m}$ -wide waveguide. Adiabatic tapers between the hybrid and passive waveguide are used to prevent the excitation of higher order modes in the passive waveguide.

The process consists of three major parts: a prebond step, the bonding step, and the III–V processing. In the prebond step, the rib waveguides are defined by *i*-line lithography. The pattern is transferred into an SiO<sub>2</sub> hard mask, and then into the silicon layer by dry etching. Next, vertical outgassing channels are etched in the silicon to improve the III–V adhesion to the silicon as explained in [10]. In the bonding step, the III–V and SOI samples are treated in an O<sub>2</sub> plasma followed by a surface treatment in NH<sub>4</sub>OH. Finally, the III–V sample is brought into physical contact with the silicon sample and the samples bond spontaneously. The bonded sample is annealed at 300 °C for 1 h at a pressure of 3 MPa as that pressure has been found to be necessary to overcome the expansion of air trapped in verti-

TABLE I  
SUMMARY OF THE III–V EPITAXIAL LAYER STRUCTURE  
USED FOR THE AWG LASER

Layer	Material	Thickness
P contact	In <sub>0.53</sub> Ga <sub>0.47</sub> As	100 nm
Cladding	InP	1.5 $\mu\text{m}$
SCH	AlGaInAs	125 nm
Quantum wells/barriers	AlGaInAs (well) (8x) AlGaInAs (barrier) (9x)	7 nm 8 nm
SCH	AlGaInAs	125 nm
N contact	InP	110 nm
Superlattice	In <sub>0.85</sub> Ga <sub>0.15</sub> As <sub>0.327</sub> P <sub>0.773</sub> (2x) InP (2x)	7.5 nm 7.5 nm
Bonding	InP	10 nm
Waveguide	Si	700 nm
Buried Oxide	SiO <sub>2</sub>	1 $\mu\text{m}$
Substrate	Si	600 $\mu\text{m}$

cal outgassing channels. As the III–V sample has no patterns, bonding alignment is not critical. During the III–V processing, a mesa is etched in the III–V and metal contacts are deposited. A current channel is defined by proton implantation to ensure that carriers recombine close to the optical mode, thus providing gain to the mode of interest. The current channel is 4  $\mu\text{m}$  wide as previous studies have shown it to give the highest injection efficiency [11].

The layer stack of the fabricated device is summarized in Table I. There are eight quantum well layers with separate confinement heterostructure layers on either side. The overlap of the optical mode with the quantum wells is 8%. AlGaInAs was chosen as the material for the quantum wells, as it gives better high-temperature performance than InGaAsP quantum wells [12].

As shown in Fig. 2, the fundamental mode in the hybrid silicon region is different from that in the passive region. To insure minimal reflections and a high coupling efficiency, adiabatic tapers on three etch levels are used to transition the mode from hybrid to passive regions. See Fig. 3 for a schematic drawing of the taper. Simulations predict that  $7.1 \times 10^{-5}$  % of the fundamental mode in the 2- $\mu\text{m}$ -wide waveguide will be reflected by the taper. While these simulations do take a finite taper tip width of 500 nm into account, the reflectivity is expected to be larger because of sidewall roughness in the taper. The simulations also show that 93.8% of the fundamental mode in the passive waveguide will couple to the fundamental mode of the hybrid waveguide. The remaining 6.2% are coupled to higher order modes, which see less gain in the SOA, so only the fundamental mode will lase. Previous studies on similar tapers on this platform have shown taper losses to be on the order of 1 dB [13].

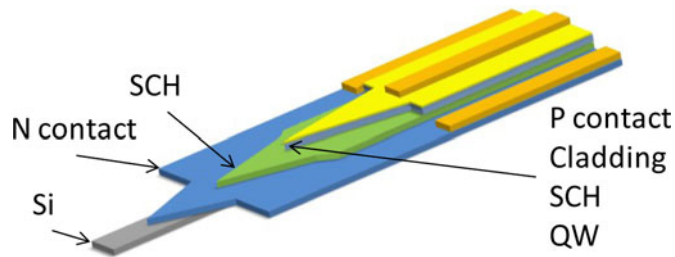


Fig. 3. Taper structure used to transition the mode from the passive region (lower left) to the hybrid region (upper right). The silicon waveguide width in the passive region is  $2\ \mu\text{m}$ , while in the hybrid region it is  $1\ \mu\text{m}$ .

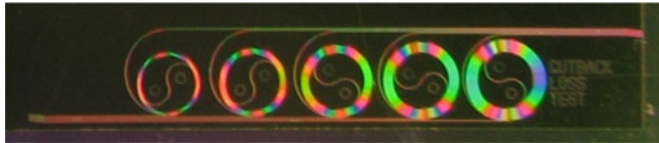


Fig. 4. Cutback test structure to extract the loss of the passive waveguide.

### III. DEVICE CHARACTERIZATION

We start by characterizing the individual components that the AWG laser consists of the waveguide, the AWG, and the SOA. We will then discuss the performance of the AWG laser.

#### A. Waveguide Losses

The waveguide loss of the  $2\text{-}\mu\text{m}$ -wide waveguides was measured using a cutback structure located on the same chip. A photograph of these structures is shown in Fig. 4. The structure consists of five waveguides with lengths of 2, 4, 6, 8, and 10 cm. Broadband amplified spontaneous emission (ASE) light centered at 1550 nm was coupled into waveguides, and the transmission powers were measured. A straight line fit through these data gave a propagation loss of 2 dB/cm before bonding. The propagation loss of the finished devices was  $\sim 2.5$  dB/cm. The propagation loss in the passive region of the AWG laser is higher than what was measured by the test structure as the test structure was protected by dielectric layers during the process. Previous process runs have consistently shown that during III–V processing, the loss increases by 1–2 dB/cm in similar waveguides. The loss of the passive waveguides in the AWG after processing was assumed to be  $\sim 4.5$  dB/cm.

The loss increase during III–V processing can be due to a number of reasons. The surface and sidewall roughnesses of the silicon waveguide can increase by the n-InP etch as this etch stops at the silicon waveguide layer. In addition, unwanted positive ion impurities such as  $\text{Na}^+$  and  $\text{K}^+$  are present to a limited extent in the cleanroom environment. When transferred to the sample, these positive ions attract free electrons in the waveguide leading to free carrier loss as explained by [14].

Atomic force microscope scans showed that the RMS surface roughness of silicon waveguides that are initially covered by III–V but at the end of the process are exposed to air increases from 0.25 to 0.36 nm. The effect this has on loss is not known at this point. Furthermore, secondary ion mass spectroscopy showed a large amount of  $\text{Na}^+$  ions at the top of the waveguides.

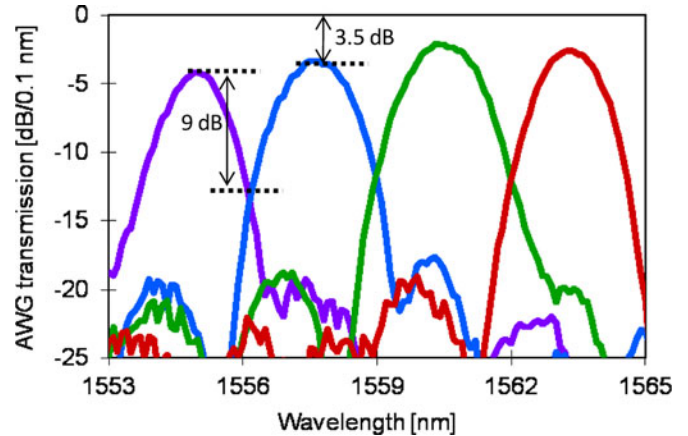


Fig. 5. AWG transmission for randomly polarized light. The average insertion loss and crosstalk are 3.5 and 9 dB, respectively.

These impurities can account for an increase of  $\sim 0.5$  dB/cm due to free carrier loss. For applications that require low-loss waveguides, it is critical to protect the waveguides during the III–V process. Ideally, III–V material should only be bonded in the area where active elements will be defined, while the rest of the chip should be covered by a hard mask that protects the waveguides during the III–V etches and that acts as a  $\text{Na}^+$  diffusion-blocking layer.

Plasma-enhanced chemical vapor deposition (PECVD)  $\text{Si}_3\text{N}_4$  has been shown to be an effective  $\text{Na}^+$ -blocking layer as shown in [15]; however, it has an index of 2.1 at 1550 nm that will lead to reflections between waveguides covered by SU8 ( $n = 1.56$ ) and waveguides covered by  $\text{Si}_3\text{N}_4$ . As a result, waveguides that must be kept low loss are covered by 700 nm of PECVD  $\text{SiO}_2$  ( $n = 1.45$ ) and 700 nm of  $\text{Si}_3\text{N}_4$  on top of the  $\text{SiO}_2$ .

On a separate fabrication run, the cutback structures were protected in this new fashion and the chips went through the same process as the AWG laser. The silicon wafers differed from the AWG laser run in that the rib etch was  $0.4\ \mu\text{m}$  and the etch was done by Numonyx/Intel Corp. Before bonding, their losses were measured to be 0.4 dB/cm while the losses of the finished devices were 0.6 dB/cm. The results show that passive waveguides should be protected during III–V processing to preserve low losses. The origin of the additional loss increase of 0.2 dB/cm is unknown at this time.

#### B. Passive AWG Performance

To quantify the AWG, a reference AWG with the same design from the same chip was measured. The transmission characteristics of randomly polarized light after the waveguide etch are shown in Fig. 5. The crosstalk and insertion loss were measured to be 9 and 3.5 dB, respectively, in good agreement with simulations. The crosstalk can be improved by increasing the number of arms, but as a laser filter 9 dB of crosstalk is sufficient to prevent one channel from lasing in another channel as the material gain does not vary by more than 9 dB from one channel to another.

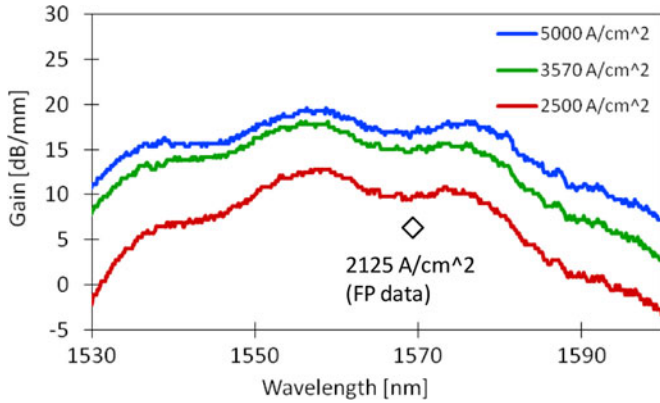


Fig. 6. Gain test structures showed a peak gain of 19 dB for a 1-mm-long SOA around 1560 nm at an injection current density of 5 kA/cm<sup>2</sup> and a stage temperature of 17 °C. The diamond data point was extracted from a Fabry–Perot laser.

### C. SOA Performance

The gain of the SOA was determined using a method similar to the contacted segment method as described by [16]. Here, SOAs with lengths  $L$ ,  $2L$ ,  $4L$ , and  $8L$  ( $L = 100 \mu\text{m}$ ) were fabricated. These SOAs differ from the SOAs in the AWG laser in that one of the output waveguides is terminated such that light from the SOA is coupled into the silicon slab. The other end of the SOA couples light into a passive waveguide. ASE is then collected by a lensed fiber. The gain of the SOA can be extracted by measuring the ASE spectra of two different SOAs at the same current density  $J$  and by applying.

$$G - \alpha_i = \frac{1}{L} \ln \left( \frac{I(2L)}{I(L)} - 1 \right) \quad (1)$$

where  $G$  is the modal gain,  $\alpha_i$  the mode loss, and  $L$  is the length of the SOA.  $I(2L)$  and  $I(L)$  are the ASE spectra of the SOAs with length  $2L$  and  $L$ , respectively, and they have units of watts per nanometer. Since two different devices had to be measured to extract the gain, we assumed that the chip-to-fiber coupling was the same for both devices.

Fig. 6 shows the data that were collected by comparing an 800- $\mu\text{m}$  SOA with a 400- $\mu\text{m}$ -long SOA at three different injection current densities. A peak gain of  $\sim 19$  dB/mm SOA length is seen around 1560 nm at an injection current density of 5 kA/cm<sup>2</sup>. We hypothesize that the supermodulation is due to multimoding behavior in the SOA.

A Fabry–Perot laser with a 1-mm-long gain section showed threshold at a current of 85 mA and it started lasing at 1570 nm. From these data, additional gain data can be extracted. Threshold is defined as the point where the roundtrip loss is overcome by the roundtrip gain of the device. The roundtrip loss of this device is 6.6 dB, and it is overcome at a current of 85 mA, or 2125 A/cm<sup>2</sup> (1-mm-long SOA, 4- $\mu\text{m}$ -wide current channel). This data point is plotted by a diamond in Fig. 6.

### D. AWG Laser Performance

The AWG transmission spectrum of the finished device is shown in Fig. 7. These data were collected by forward biasing

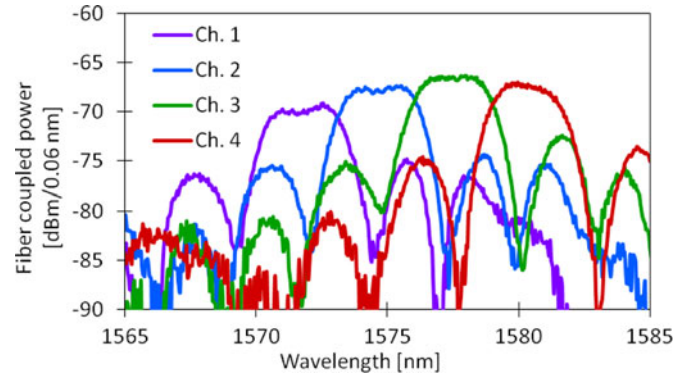


Fig. 7. ASE output of the common output waveguide for an SOA bias of 75 mA.

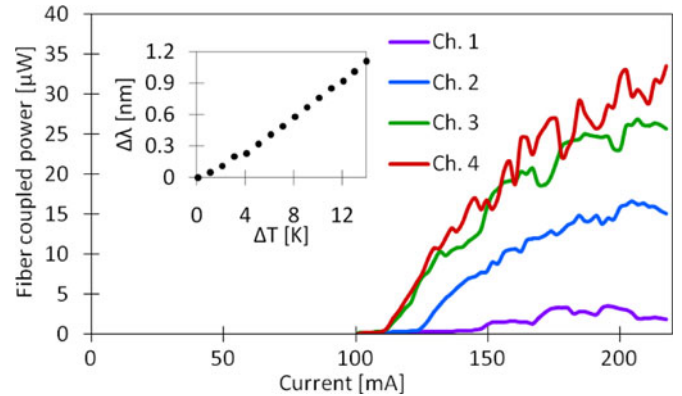


Fig. 8. Continuous wave  $L$ - $I$  curve for the four channels at a stage temperature of 17 °C. Lasing thresholds are between 113 and 147 mA. The inset shows the change in lasing wavelength as the stage temperature is raised.

one amplifier at a time below threshold (at 75 mA and measuring the output of the common output waveguide fc, [see Fig. 1(b)], with an optical spectrum analyzer. The reason the AWG passbands degraded is because some of the III–V that was covering the AWG did not adhere to the silicon. Subsequent etch steps that were supposed to etch the III–V were etching the silicon, thus attacking certain phase arms and the free propagating region. In future device runs, this will be prevented by not bonding III–V to the AWG and protecting the AWG with SiO<sub>2</sub> and Si<sub>3</sub>N<sub>4</sub> as discussed earlier.

Even though the passbands of the AWG were attacked, which introduced losses, all four channels lased. Fig. 8 shows continuous wave (CW) lasing thresholds between 113 and 123 mA for Channels 2–4, while Channel 1 has a higher threshold of just under 150 mA. For these measurements, the chip was mounted on a thermoelectric cooler that was set to 17 °C. The higher threshold in channel 1 is a result of a poorer AWG transmission in that channel as shown in Fig. 5.

The maximum single-sided fiber-coupled output power is 35  $\mu\text{W}$ . Taking chip-to-fiber coupling losses into account ( $\sim 9.5$  dB), the output power from the common facet is about 0.3 mW. The output power can be almost doubled by applying a high-reflection coating on one side of the chip.

Fabry–Perot lasers from the same chip with an identical SOA design but without an AWG showed lasing thresholds of 85 mA

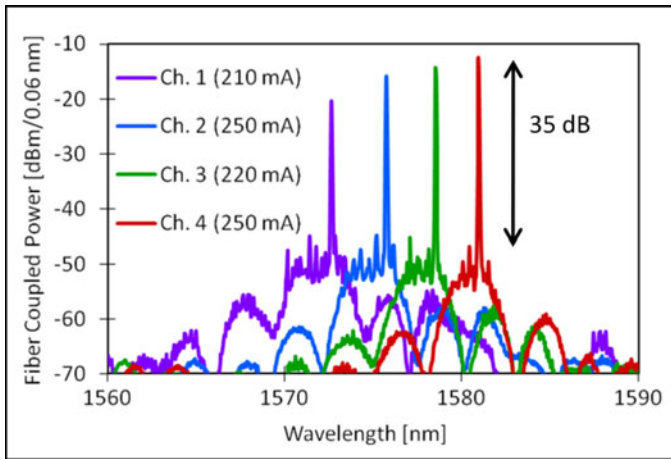


Fig. 9. Optical spectrum of the four channels optimized for maximum SMSR.

on the same chip. Data from our gain test structures show that the difference in threshold translates to an additional 6 dB of loss inside the AWG laser. Of those 6 dB, 3.5 dB are due to the insertion loss of the AWG laser. The additional 2.5 dB are due to taper losses and process-induced losses. This suggests that the lasing threshold of the AWG laser can be significantly reduced by decreasing the insertion loss of the AWG. One approach would be to use a vertical taper as demonstrated by [17]. The threshold can be further reduced by protecting the AWG during the III–V etching, thus reducing process-induced losses.

The inset in Fig. 8 shows the lasing wavelength of Channel 4 as a function of stage temperature. CW lasing operation up to 30 °C is seen, and a temperature-dependent wavelength shift of 0.08 nm/K is observed. This shift is due to the gain peak shift and the shift of the AWG passband. To separate the two effects, the temperature-dependent wavelength shift of a Fabry–Perot laser from the same chip without an AWG was tested. The Fabry–Perot laser showed a shift of 0.06 nm/K that is entirely due to the gain peak shift. This means that the remaining shift of 0.02 nm/K is entirely due to the AWG. The data show that for applications where wavelength stability is required, an AWG laser needs to be kept at a constant temperature. At the same time, the lasing wavelength of the device can be accurately controlled by adjusting the temperature.

The optical spectrum of all four channels is shown in Fig. 9. The currents in the SOAs were tuned to maximize the side-mode suppression ratio (SMSR). Channel 4 has the highest SMSR of 35 dB. The channels with flatter passbands have a lower SMSR. Properly protecting the AWG during the III–V etching will preserve the passbands (there will be a well-defined peak) that will improve the SMSR in all channels.

Fig. 8 shows kinks in the  $L$ – $I$  curve of all devices. This can be due to mode hopping. To investigate this, we take the spectrum at the same time as we measure the  $L$ – $I$  curve. In Fig. 10(a), the  $L$ – $I$  curve of Channel 2 is plotted, while the contour plot of the optical spectrum as a function of injection current is plotted in Fig. 10(b); a clear relationship between kinks in the  $L$ – $I$  curve and mode hops in the optical spectrum is seen as indicated by the dashed lines.

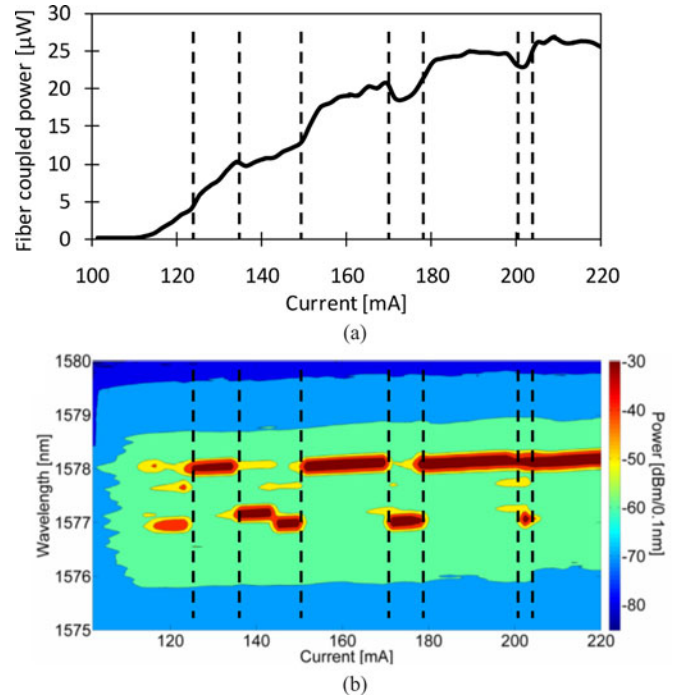


Fig. 10. Contour plot of the optical spectrum (a) is shown on the same horizontal axis as the  $L$ – $I$  curve (b) for Channel 3. The kinks in the  $L$ – $I$  curve are due to mode hops. The current resolution is 2 mA. The gradual slope of the lasing mode is due to the self-heating of the device.

The mode hopping arises because the passbands of the AWG flattened out during the process as described earlier, creating a  $\sim 3$ -nm-wide band of approximately uniform transmission. The 3-nm-wide flat passband in combination with the free spectral range (FSR) of the cavity (0.07 nm) make it possible to have multiple modes lasing simultaneously and it is observed in all the channels in this device at various drive currents. Even though the FSR of the cavity is 0.07 nm, the modes jump by  $\sim 1$  nm, corresponding to a cavity of  $\sim 293 \mu\text{m}$  or an integer multiple thereof. We hypothesize that this unintended cavity is formed by one of the AWG arms that is 1200  $\mu\text{m}$  ( $\sim 4$  times 293  $\mu\text{m}$ ) long, thus supermodulating the expected Fabry–Perot response and allowing these 1-nm jumps.

When the AWG passbands have a shape as in Fig. 5, multimoding and mode hopping should be suppressed. In addition, the cavity can be made shorter to increase the FSR of the cavity, thus supporting fewer modes near the peak of the passband.

This device can be used as a discretely tunable laser. Direct modulation of Channel 4 showed rise and fall times of 190 and 240 ps as shown in Fig. 11. However, during turn on and turn off, the laser can mode hop that can be an issue in a WDM system.

For this device to be useful as a transmitter, it needs to be able to transmit modulated signals. Direct modulation at 1 GHz showed an open eye and an extinction ratio of 7.8 dB as shown in Fig. 12. Open eyes up to 2.5 GHz were observed but the extinction ratio degraded to 3 dB. A better way to modulate the signal in this device is to integrate modulators using a configuration as shown in Fig. 13 as proposed by [18]. By integrating the

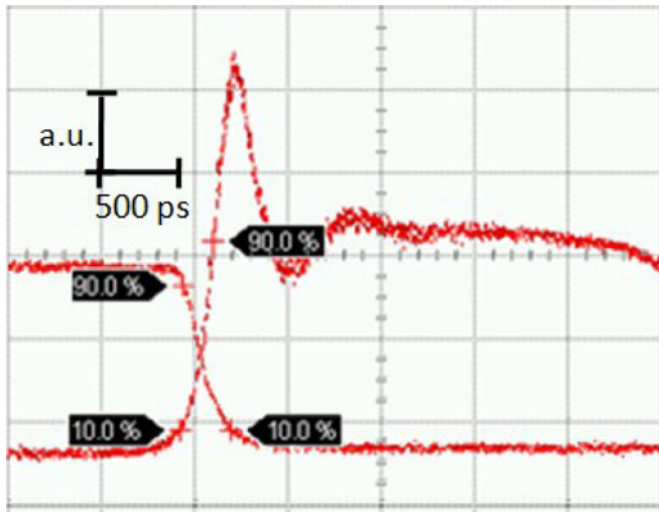


Fig. 11. (a) Turn-on and (b) turn-off characteristics of the AWG laser.

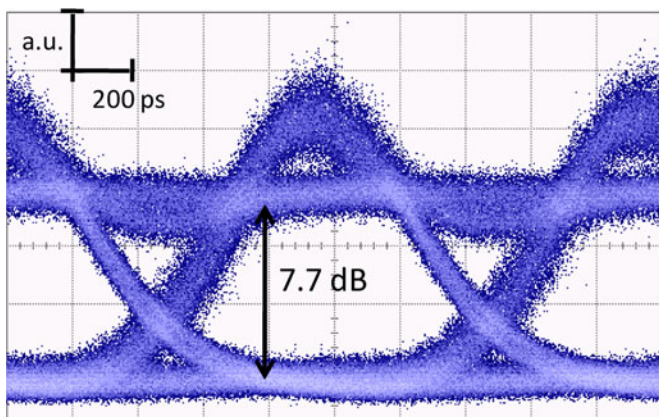


Fig. 12. Eye diagram of Channel 4 with direct modulation at 1 GHz. An extinction ratio of 7.7 dB is measured. The extinction ratio degraded to 3 dB at 2.5 GHz.

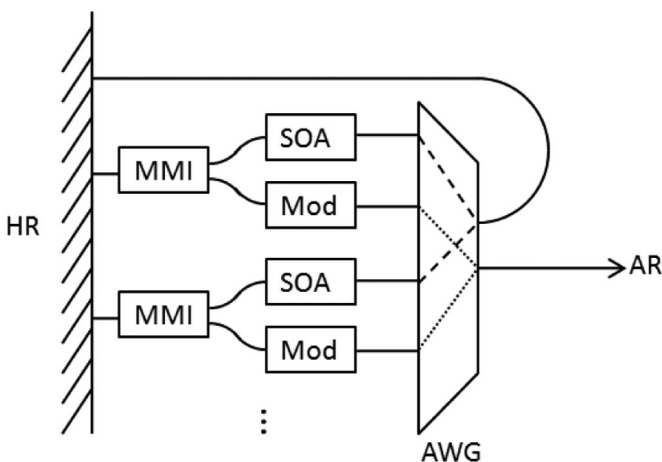


Fig. 13. Proposed layout for an MWL with integrated modulators.

modulators outside of the lasing cavity, the modulation speed will not be limited by the length of the cavity. One way is to bond a separate epitaxial layer with shifted quantum wells, and

then define modulators. An easier way is to use quantum well intermixing to shift the gain peak in certain regions of the III–V wafer before bonding. This way, modulators can be fabricated in one gain region, while amplifiers are defined in another gain region and only one bond is required. See [19] and [20] for more details on the integration of multiple bandgaps on one III–V wafer. Alternatively, compact ring modulators as outlined in [21] can be used to modulate the signal.

#### IV. CONCLUSION

In this paper, the first hybrid silicon AWG-based MWL was presented. The device is potentially useful as a WDM light source. While the device in this paper was limited to four channels, it can be easily scaled up to several tens of channels as mature CMOS-manufacturing technology allows the fabrication of high-quality AWGs on SOI. The device is simple to operate as lasing wavelengths are selected by the AWG that is a passive element. A well-behaved temperature dependence allows the fine tuning of the lasing wavelength by adjusting the chip temperature up to 30 °C.

The performance of this device was limited as certain process steps attacked the AWG that degraded the passbands. Protecting the AWG with dielectric layers during the III–V processing will preserve the passbands of the AWG. By doing so, various device characteristics can be improved. The threshold current can be reduced to  $\sim 100$  mA. Well-preserved passbands will also eliminate mode hopping, and they will give a more uniform channel spacing.

#### ACKNOWLEDGMENT

The authors would like to thank H.-W. Chen and J. Bauters for dicing samples. The silicon and vertical outgassing channel etching on the reference wafers were done by Numonyx/Intel under the supervision of Dr. R. Jones and Dr. H. Bar. They are also grateful to Prof. Z. Wang for helping measuring the transmission of the passive AWG, M. V. Westeinde for the taper simulations, and S. Jain and H.-W. Chen for fruitful discussions on device testing.

#### REFERENCES

- [1] G. Roelkens, L. Liu, D. Liang, R. Jones, A. W. Fang, B. Koch, and J. E. Bowers, "III-V/silicon photonics for on-chip and intra-chip optical interconnects," *Laser Photon. Rev.*, vol. 4, pp. 1–29, 2010.
- [2] D. A. B. Miller, "Device requirements for optical interconnects to silicon chips," *Proc. IEEE*, vol. 97, no. 7, pp. 1166–1185, Jul. 2009.
- [3] M. Haurylau, G. Chen, H. Chen, J. Zhang, N. A. Nelson, D. H. Albonese, E. G. Friedman, and P. M. Fauchet, "On-chip optical interconnect roadmap: challenges and critical directions," *IEEE J. Select. Top. Quantum. Electron.*, vol. 12, no. 6, pp. 1699–1705, Nov./Dec. 2006.
- [4] J. H. den Besten, R. G. Broeke, M. van Geemert, J. J. M. Binsma, F. Heinrichsdorff, T. van Dongen, E. A. J. M. Bente, X. J. M. Leijtens, and M. K. Smit, "An integrated 4×4-channel multiwavelength laser on InP," *IEEE Photon. Technol. Lett.*, vol. 15, no. 3, pp. 368–370, Mar. 2003.
- [5] A. A. M. Staring, L. H. Spiekman, J. J. M. Binsma, E. J. Jansen, T. van Dongen, P. J. A. Thijs, M. K. Smit, and B. H. Verbeek, "A compact nine-channel multiwavelength laser," *IEEE Photon. Technol. Lett.*, vol. 8, no. 9, pp. 1139–1141, Sep. 1996.
- [6] J. H. den Besten, D. Caprioli, R. van Dijk, F. E. van Vliet, W. Pascher, J. J. M. Binsma, E. Smalbrugge, T. de Vries, R. G. Broeke, Y. S. Oei, E. A. J. M. Bente, X. J. M. Leijtens, and M. K. Smit, "Integration of MZI

modulators and AWG-based multiwavelength lasers in InP," presented at the Proc. Symp. IEEE/LEOS Benelux Chapter, Ghent, Belgium, 2004.

- [7] W. Bogaerts, R. Baets, P. Dumon, V. Wiaux, S. Beckx, D. Taillaert, B. Luysaert, J. V. Campenhout, P. Bienstman, and D. V. Thourhout, "Nanophotonic waveguides in silicon-on-insulator fabricated with CMOS technology," *J. Lightw. Technol.*, vol. 23, no. 1, pp. 401–412, Jan. 2005.
- [8] P. Cheben, J. H. Schmid, A. Del age, A. Densmore, S. Janz, B. Lamontagne, J. Lapointe, E. Post, P. Waldron, and D.-X. Xu, "A high-resolution silicon-on-insulator arrayed waveguide grating microspectrometer with sub-micrometer aperture waveguides," *Opt. Exp.*, vol. 15, no. 5, pp. 2299–2306, 2007.
- [9] A. W. Fang, M. N. Sysak, B. R. Koch, R. Jones, E. Lively, Y. -H. Kuo, D. Liang, O. Rada, and J. E. Bowers, "Single-wavelength silicon evanescent lasers," *IEEE J. Select. Top. Quantum. Electron.*, vol. 15, no. 3, pp. 535–544, May 2009.
- [10] D. Liang and J. E. Bowers, "Highly efficient vertical outgassing channels for low-temperature InP-to-silicon direct wafer bonding on the silicon-on-insulator substrate," *J. Vac. Sci. Technol. B*, vol. 26, no. 4, pp. 1560–1568, Jul. 1, 2008.
- [11] M. Sysak, Intel Corporation, Santa Clara, CA, private communication, Jun. 2009.
- [12] C. E. Zah, R. Bhat, B. N. Pathak, F. Favire, W. Lin, M. C. Wang, N. C. Andreadakis, D. M. Huang, M. A. Koza, T. P. Lee, Z. Wang, D. Darby, D. Flanders, and J. J. Hsieh, "High-performance uncooled 1.3- $\mu\text{m}$   $\text{Al}_x\text{Ga}_y\text{In}_{1-x-y}\text{As}/\text{InP}$  strained-layer quantum-well lasers for subscriber loop applications," *IEEE J. Quantum Electron.*, vol. 30, no. 2, pp. 511–523, Feb. 1994.
- [13] H. Park, Y.-H. Kuo, A. W. Fang, R. Jones, O. Cohen, M. J. Pannicia, and J. E. Bowers, "A hybrid AlGaInAs-silicon evanescent preamplifier and photodetector," *Opt. Exp.*, vol. 15, no. 21, pp. 13539–13546, Oct. 2007.
- [14] R. Soref and B. Bennett, "Electrooptical effects in silicon," *IEEE J. Quantum Electron.*, vol. 23, no. 1, pp. 123–129, Jan. 1987.
- [15] Y. Nishi and R. Doering, *Handbook of Semiconductor Manufacturing Technology*. Boca Raton, FL: CRC Press, 2007, p. 325.
- [16] P. Blood, G. M. Lewis, P. M. Smowton, H. D. Summers, J. Thomson, and J. Lutti, "Characterisation of semiconductor laser gain media by the segmented contact method," *IEEE Select. Top. Quantum. Electron.*, vol. 9, no. 5, pp. 1275–1282, Sep/Oct. 2003.
- [17] A. Sugita, A. Kaneko, K. Okamoto, M. Itoh, A. Himeno, and Y. Ohmori, "Very low insertion loss arrayed-waveguide grating with vertically tapered waveguides," *IEEE Photon. Technol. Lett.*, vol. 12, no. 9, pp. 1180–1182, Sep. 2000.
- [18] J. Zhao, X. Leijtens, B. Docter, and M. Smit, "Integrated multi-wavelength lasers: A design study," in *Proc. Symp. IEEE Photon. Benelux Chapter*, Brussels, Belgium, 2009, pp. 209–212.
- [19] S. Jain, M. N. Sysak, G. Kurczveil, and J. E. Bowers, "Integration of hybrid silicon DFB laser and electro-absorption modulator using quantum well intermixing," presented at the Eur. Conf. Opt. Commun., Torino, Italy, Sep. 19–23, 2010.
- [20] J. W. Raring, E. J. Skogen, L. A. Johansson, M. N. Sysak, J. S. Barton, M. L. Masanovic, and L. A. Coldren, "Quantum well intermixing for monolithic integration: A demonstration of novel widely-tunable 10 Gb/s transmitters and wavelength converters," presented at the Integr. Photon. Res. Conf., IWC3, San Francisco, CA, Jun. 2004.
- [21] L. Zhang, Y. Li, J.-Y. Yang, M. Song, R. G. Beausoleil, and A. E. Willner, "Silicon-based microring resonator modulators for intensity modulation," *IEEE J. Select. Top. Quantum. Electron.*, vol. 16, no. 1, pp. 149–158, Jan./Feb. 2010.



**G za Kurczveil** received the B.S. degree in physics from the University of California, Santa Cruz, in 2006, and the M.S. degree in electrical and computer engineering from the University of California, Santa Barbara (UCSB), in 2009, where he is currently working toward the Ph.D. degree in electrical and computer engineering.

His research interests include integrated optical buffers and the integration of low-loss waveguides with active devices on silicon.



**Martijn J. R. Heck** (S'04–M'09) received the M.Sc. degree in applied physics, and the Ph.D. degree from the Eindhoven University of Technology, Eindhoven, The Netherlands, in 2002 and 2008, respectively.

From 2007 to 2008, he was a Postdoctoral Researcher at the Communication Technology: Basic Research and Applications Research Institute, Eindhoven University of Technology, where he was engaged in the development of a technology platform for active-passive integration of photonic integrated circuits. From 2008 to 2009, he was with Laser Centre, Vrije Universiteit, Amsterdam, The Netherlands, where he was involved in the development of integrated frequency-comb generators. He is currently a Postdoctoral Researcher in the Department of Electrical Engineering, University of California, Santa Barbara, where he is involved in photonic integrated circuits based on the heterogeneous integration of silicon photonics with III/V materials.



**Jonathan D. Peters** has more than 13 years of process experience in the microelectromechanical systems and semiconductor field. He was with the Applied Magnetics Corporation, Santa Barbara, CA, as an Operator, Process Inspector, and Plate and Etch Technician for five years before joining Solus Micro Technologies/NP Photonics, Westlake Village, as a Process Engineer for four years. He then joined Innovative Micro Technology, Santa Barbara, as a Process Engineer and Research and Development Engineer for four years. In 2008, he joined the Department of Electrical and Computer Engineering, University of California, Santa Barbara.



**John M. Garcia** received the B.S. degree in computer science, in 2007, and the M.S. degree in electrical and computer engineering in 2009 from the University of California, Santa Barbara, where he is currently working toward the Ph.D. degree in electrical and computer engineering.

His research interests include optical networks, optical packet switching, and optical packet routing.



**Daryl Spencer** received the B.S. degree in engineering physics from the University of Tulsa, Tulsa, OK, in May 2010. He is currently working toward the M.S./Ph.D. degrees in electrical and computer engineering at the University of California, Santa Barbara, as a Holbrook Foundation Fellow.



**John E. Bowers** (F'93) received the M.S. and Ph.D. degrees from Stanford University, Stanford, CA, in 1978 and 1981, respectively.

He was with AT&T Bell Laboratories and Honeywell before joining University of California, Santa Barbara (UCSB). He currently holds the Fred Kavli Chair in Nanotechnology. He is the Director of the Institute for Energy Efficiency, and a Professor in the Department of Electrical and Computer Engineering at UCSB. He is a cofounder of Aurion, Aerius Photonics and Calient Networks. He has published eight

book chapters, 450 journal papers, 700 conference papers and has received 52 patents.

Dr. Bowers is a member of the National Academy of Engineering, a Fellow of the OSA and the American Physical Society, and a recipient of the OSA Holonyak Prize, the IEEE LEOS William Streifer Award and the South Coast Business and Technology Entrepreneur of the Year Award. He and coworkers received the EE Times Annual Creativity in Electronics (ACE) Award for Most Promising Technology for the hybrid silicon laser in 2007.